
Article:
Saleh, M.N. orcid.org/0000-0002-0725-5319, Yudhanto, A., Lubineau, G. et al. (1 more author) (2017) The effect of z-binding yarns on the electrical properties of 3D woven composites. Composite Structures, 182. pp. 606-616. ISSN 0263-8223

https://doi.org/10.1016/j.compstruct.2017.09.081

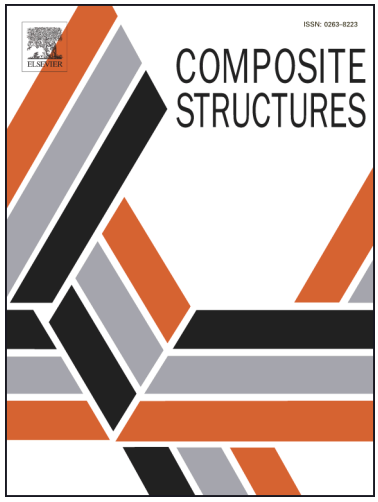

The effect of z-binding yarns on the electrical properties of 3D woven composites

Mohamed Nasr Saleh, Arief Yudhanto, Gilles Lubineau, Constantinos Soutis

PII: S0263-8223(17)31618-5
DOI: https://doi.org/10.1016/j.compstruct.2017.09.081
Reference: COST 8944

To appear in: *Composite Structures*

Received Date: 23 May 2017
Revised Date: 9 August 2017
Accepted Date: 26 September 2017

Please cite this article as: Saleh, M.N., Yudhanto, A., Lubineau, G., Soutis, C., The effect of z-binding yarns on the electrical properties of 3D woven composites, *Composite Structures* (2017), doi: https://doi.org/10.1016/j.compstruct.2017.09.081

The effect of z-binding yarns on the electrical properties of 3D woven composites

Mohamed Nasr Saleh[1], Arief Yudhanto[2], Gilles Lubineau[2], Constantinos Soutis[3]

[1]Advanced Manufacturing Research Centre with Boeing, University of Sheffield, Rotherham, S60 5TZ, UK

[2]King Abdullah University of Science and Technology (KAUST), Physical Sciences and Engineering Division, COHMAS Laboratory, Thuwal 23955-6900, Saudi Arabia

[3]Aerospace Research Institute, University of Manchester, M1 3NJ, UK.

Abstract

Electrical resistance monitoring (ERM) has been used to study the effect of the z-binding yarns on the initial electrical resistance (ER) and its change of three architectures of 3D woven carbon fibre composites namely (orthogonal "ORT", layer-to-layer "LTL" and angle interlock "AI") when tested in tension. Specimens are loaded in on-axis "warp" and off-axis "45º" directions. *In-situ* ERM is achieved using the four-probe technique. Monotonic and cyclic "load/unload" tests are performed to investigate the effect of piezo-resistivity and residual plasticity on resistance variation. The resistance increase for the off-axis loaded specimens (~90%) is found to be higher than that of their on-axis counterparts (~20%). In the case of cyclic testing, the resistance increase upon unloading is irreversible which suggests permanent damage presence not piezo-resistive effect. At the moment, it is difficult to obtain a direct correlation between resistance variation and damage in 3D woven composites due to the complexity of the conduction path along the three orthogonal directions, however this study demonstrates the potential of using ERM for damage detection in 3D woven carbon fibre-based composites and highlights the challenges that need to be overcome to establish ERM as a Structural Health Monitoring (SHM) technique for such material systems.

Keywords: Carbon fibres, 3-Dimensional reinforcement, Electrical properties, Damage mechanics

1 Introduction

Automation in textile technology has been, recently, adopted to produce cost-effective three-dimensional (3D) woven preforms using engineered fibres such as carbon and glass with high strength/modulus. The cost of manufacturing 3D composites is lower than that of producing 2D composites [1] as it can produce near net shapes with reduced material scrap. In addition, 3D woven composites exhibit higher impact resistance, post-impact strength and delamination resistance compared to classical 2D laminates [2–6]. This enhancement in properties mainly results from the introduction of through-thickness binding yarns which improve the out-of-plane properties compared to 2D laminated composite systems but at the same time compromise the in-plane properties due to yarns' undulations [7–9].

Detecting and monitoring damage in composites are challenging tasks because damage can consist of different interactive modes, while its progression is dependent on the damage type. Damage modes in composites can be generally grouped into two categories: first, intra-laminar cracking (diffused damage [10], transverse cracking [11–13], local delamination [14–16], fibre breakage [17,18]) and second, inter-laminar damage (delamination or separation between plies/yarns [19,20]). Detecting damage in 3D woven composites is even more challenging since the z-binding yarns also contribute to the damage initiation and development [9,19–24]. Due to the high stress concentration at the interlacement points between z-binding yarns and in-plane yarns, localised damage occurs at those locations. Furthermore, the progression of delamination is also controlled by the architecture of z-binding yarns in 3D composites [23,25,26]. Having a reliable real-time damage detection technique is essential for monitoring the integrity of 2D laminated and 3D woven composites in service especially for the non-visible damage that may lead to catastrophic failure. Structural Health Monitoring (SHM) techniques such as ultrasonic [27], optical fibres [28], acoustic emission [29] and lamb waves [30,31] have been widely used for damage detection in composites.

One alternative method for monitoring damage, particularly in carbon-based composites, is electrical resistance (ER) measurement where the change of resistance is correlated with damage accumulation. ERM of unidirectional composites [32–34] during

monotonic and cyclic "load/unload" tensile testing have proved the potential of this technique in *in-situ* detection and tracking of damage in carbon based composites. Change in resistivity has already been correlated with different non-reversible damage mechanisms (matrix cracking, transverse cracking and fibre breakage) [34–38] or reversible negative piezo-resistivity due to fibre alignment [34,38,39]. Damage monitoring as function of resistance change has been extended to delamination detection in flexural testing in [33,38]. Moreover, Hirano and Todoroki [35] and Berry [36] have successfully used ERM technique to detect damage in 2D woven composites.

To date, the feasibility of ERM in 3D woven composites has not been investigated. To the best of the authors' knowledge, no correlation has been made between damage (initiation as well as its progression) and ER in 3D woven composites. At the moment, it is very difficult to obtain a direct correlation between resistance variation and damage in 3D woven composites due to the complexity of the conduction path along the three orthogonal directions (x, y & z). Thus, this study represents a first attempt to demonstrate the potential of using ERM for damage detection in 3D woven carbon fibre composites and highlight the challenges that need to be overcome to establish ERM as a SHM technique for such material systems. In addition, no investigation of the effect of the z-binding yarns on the electrical conductivity of 3D woven composites has been reported. This research work extends the work on damage detection using ERM that has been performed on 2D laminated composites [34–36,40–43] to capture the effect of the z-binding yarns in 3D woven composites. Monotonic and cyclic tensile tests are performed to study the effect of loading-direction and residual plasticity on ER of 3D woven composites. Three architectures of 3D woven composites are investigated here orthogonal (ORT), layer-to-layer (LTL) and angle interlock (AI). Those materials are loaded in tension along (i) warp (0^o) and bias (45^o) directions. Global stress-strain curves are evaluated along with resistance variation due to damage initiation and accumulation. In addition, advantages and limitations of the ERM technique are also discussed.

This paper is divided into five sections. Section 2 details the 3D woven architectures and composite manufacturing. Section 3 describes the specimens' preparation process and test setup (tensile test coupled with digital image correlation and four-probe electrical

measurement). Section 4 details the results and discusses the significance of the experimental observations (effect of z-binder on the initial resistance, resistance variation upon loading for on-axis and off-axis tested specimens as well as residual plasticity and piezo-resistivity in off-axis monotonic and cyclic tests). Finally, section 5 summarises the main concluding remarks of the paper and discusses the limitations of the proposed technique.

2 Materials and manufacturing

The carbon fibre used in this study is HexTow IM7 (Hexcel), while the epoxy is MTM 57 (medium temperature epoxy produced by Solvay). The dry 3D woven fabrics were produced by Sigmatex UK. Fig. 1 shows the schematics of 3D woven fabrics drawn using TexGen software [44]. The parameters of textile architecture of 3D woven composites are given in Table 1. The in-plane fibre count (warp and weft) for ORT, AI and LTL is 12k. The z-binder fibre count for ORT, AI and LTL is 6k, 6k and 12k, respectively. The number of warp threads, weft threads and z-binder threads per unit length (in cm) is specified in Table 1 as ends/cm, picks/cm and binders/cm, respectively. In addition, the areal density of dry 3D woven fabric is also given in Table 1 (unit is g/m^2).

To produce 3D woven composite panels, the dry fabrics were infiltrated by MTM 57 epoxy matrix using resin film infusion (RFI) process. Infusion process was carried out at 70ºC for 1 h, while curing process was done at 120ºC for 1 h. Minimum curing pressure for MTM 57 was set to 2.8 bars. Once the 3D woven composite panels with the size of 300 mm x 200 mm were cured, they were cut into specimens of two different orientations, i.e. warp and off-axis. Thickness of cured composite panels ranges between 3.2 to 3.6 mm depending on the warp and weft number of layers (see Table 1).

3 Experiment and characterisation

3.1 Determination of fibre volume fraction

In this study, the determination of fibre volume fraction of the manufactured panels was conducted in two stages. The first stage deals with an experimental measurement of fibre volume fraction V_f (as well as matrix V_m and void volume fraction V_v) of samples from

the manufactured panels. The second stage deals with an analytical calculation to determine directional V_f in warp, weft and z-directions based on textile parameters given in Table 1. The procedures of both stages are described in the following sections.

3.1.1 Acid digestion

Fibre volume fraction measurement was conducted based on acid digestion technique according to ASTM D3171 standard (Constituent Content of Composite Materials). The procedure is generally described as follows: (i) specimen is immersed in the sulfuric acid where the matrix is entirely dissolved; (ii) weight of the specimen is measured before and after the digestion process. The measurement of fibre volume fraction by acid digestion also enables the measurement of the matrix volume fraction as well as void content. Readers are referred to the ASTM D3171 document for more detailed experimental and specimen requirements. Table 2 shows the fibre, matrix and void volume fractions of 3D woven composites.

3.1.2 Directional fibre volume fraction analysis

Directional fibre volume fraction analysis aims to calculate fibre volume fraction in warp, weft and z-directions, and to eventually determine the contribution of each directional fibre tows on the overall V_f. The calculation of directional V_f can be summarised as follows: first, directional areal densities of the fabric in warp, weft and z-binder direction are calculated by multiplying the yarns' count (in tex) by ends/cm, picks/cm and binders/cm, respectively. Second, the directional areal density is then normalised by the total areal density to determine the percentage of warp, weft and z-binder fibres (directional V_f). Hence, the total fibre volume fraction given in Table 2 is then divided into warp, weft and z-binder content, and Table 3 shows the so-called directional V_f. The effect of directional volume fraction on the electrical resistance is further discussed in Section. 4.1.

3.2 X-ray computed tomography

To evaluate the deviation, of the ‘‘as-manufactured” 3D woven composite panels, from the idealised geometry, X-ray CT scans were performed on the three architectures (ORT, LTL and AI) using a Zeiss Xradia VersaXRM-510 machine. For the ORT specimen, a square cross section of (30 mm x 30 mm) was cut to obtain a sufficient resolution. The 0.4x “Macro” objective of the scanner was used to get a wider field of view for such relatively

large specimens. These scanning parameters resulted in a total volume in the field of view of 10 x 10 x 10 mm^3, resulting in a voxel size of 5 µm. The source voltage and current were set to 40 kV and 75 µA respectively. The exposure time for each radiograph was 10 s, with 1600 radiographs being collected over 360º. The total data acquisition time was 7 h. Similarly, all scanning parameters were kept the same for LTL and AI except for the total volume in the field of view and consequently the voxel size. As both LTL and AI have larger unit cells, the field of view was increased to 16 x 16 x 16 mm^3 and 25 x 25 x 25 mm^3 respectively. After scanning, the 3D unit cells were reconstructed out of the 2D X-ray slices for ORT, LTL and AI. Using a cutting plane parallel to the warp yarns, X-CT section views (Fig. 2) clearly show voids and binder distortion compared to the idealised geometry defined by the schematic. This distortions can be attributed to the weaving process, RFI process and fabric compaction for all the architectures that can have impact on stiffness, damage initiation and ultimate specimen failure. Moreover, in the case of the LTL architecture (Fig. 2b), the weft layers are distorted in the vertical plane and resin rich regions are shown in black. Unlike ORT and LTL architectures, the AI architecture cross section (Fig. 2c) suggests that it has experienced the most severe binder distortion.

3.3 Specimen preparation

Test specimens (250 mm x 25 mm) were cut from the manufactured panels after tabbing process utilising glass/epoxy laminates. Afterwards, bonding of electrodes on the specimen was conducted. Four regions (5 mm wide) in the specimen were polished with sand paper (320 grit size), cleaned using acetone and treated with concentrated sulfuric acid to expose the fibres and ensure a good contact between electrodes and specimen [45]. Silver paste layers were then applied over the treated regions. The thickness of silver paste layers was typically 2 mm. Finally, conductive silver epoxy was used to bond copper wires onto the specimen surface. As depicted in Fig. 3, four probes were introduced to evaluate the resistance variation over the span of 70 x 25 mm^2 of the specimens during testing. Two outer electrodes were used to induce the current (I) while the voltage (V) difference was measured by two inner electrodes. Average initial resistance for various specimen types before testing is reported in Section. 4.1. Agilent U2741A 5.5 Digital Multi-meter was used to record the resistance.

3.4 Test procedures

3.4.1 Monotonic test

Monotonic tensile tests were carried out on on-axis (warp) and off-axis (45º) specimens of LTL, AI and ORT until the specimens failed. An Instron 5882 with a 100 kN load cell was used to apply a displacement-controlled tension with loading speed of 2 mm/min according to ASTM D3039 standard (Tensile Properties of Polymer Matrix Composite Materials). Due to material limitations, three specimens were tested for each type (ORT, LTL and AI) and each orientation (0º and 45º). All tests were performed in a controlled environment where the temperature was (21^{o}C ± 2^{o}C) and the relative humidity (RH) was (45% ± 3%). Strain was obtained using a digital image correlation (DIC) system shown in Fig. 4a. The DIC system utilised a SensiCam 12-bit CCD camera (PCO) with TC-2336 bi-telecentric lenses (The Telecentric Company). The resolution of the CCD camera was 1376 x 1040 pixels. The bi-telecentric lenses has a depth of field of 11 mm, diameter of 61 mm and magnification of 0.234 x. CamWare V3.11 software was used to capture the speckle pattern images acquired from the CCD camera. Similar settings have been successfully used for 3D woven composites, and proven to provide reasonable quality of strain fields for 3D composites [46,47]. The frame rate is set as 0.5 and 0.33 frames per second (fps) for on-axis and off-axis tensile testing, respectively. The main reason for the lower fps in off-axis tests is that the deformation up to failure in off-axis specimens is much larger than that in on-axis tests. The speckle images were then processed using Vic 2D. In processing these images, the subset size was set to a value of 101 x 101 pixels sufficient for woven composite specimens [25]. In addition, the step size (distance between subsets) was set to 5 pixels. The observation window of approximately 25 x 22 mm^2 produced an image with dimensions of 1040 x 896 pixels. Global mean values of strains (ε_{xx};ε_{yy};ε_{xy}) were obtained from DIC analysis using Vic 2D. During monotonic testing, voltage was simultaneously recorded from two inner probes (out of four probes) on the back surface as shown in Fig. 4b to calculate the resistance.

3.4.2 Cyclic test

Cyclic (load/unload) tests were conducted on off-axis specimens to evaluate residual plasticity and damage evolution and their effect on resistance variation in 3D woven composites. The loading rate was kept at 2 mm/min during cyclic loading. Five

loading/unloading cycles were applied on the specimen, and the maximum displacement for each cycle (from 1st to the 5th cycle) was 4, 8, 12, 16 and 20 mm, respectively. The minimum load defined after each unloading cycle was 100 N in order to avoid compression of the specimen.

4 Results and discussion

4.1 Measurement of initial resistance

To ensure that the measured resistance values were not just surface measurements, eight electrodes were bonded; four electrodes on each side of the specimen, and the resistance of each surface were evaluated. For all the tested specimens, the resistance obtained by injecting the current on one side "top or bottom" was found to be similar to the one measured by injecting the current on both sides simultaneously. Such resistance similarity indicates that the resistance value determined by the 4-probe technique on one surface is a representative volumetric resistance and not just a surface measurement which is attributed to the through-thickness binding yarns creating a conduction path between the top and bottom surfaces. Then, using a 4-probe technique only on one surface, the initial resistances of 3D woven specimens were measured before applying any mechanical loads. Table 4 details the measured resistance values of off-axis and on-axis specimens. The initial resistance values can be used as a baseline measurement. Influence of the z-binder yarns architecture on the resistance values can also be investigated based on the initial resistance.

Some correlation can be made between the initial resistance and the directional volume fraction. For instance, the AI architecture has the highest V_f in the warp direction which is directly translated into the least initial resistance. However, the effect of directional fibre volume fraction, especially in the case of LTL, is not definitive because the contribution of the warp yarns to the conductivity is not the only conduction path of the current. The through thickness binders also create a conduction path between the in-plane yarns as well. In other words, the binding yarns creating conduction network, between the in-plane yarns, that has an effect on the overall measured initial resistance.

It is clear that for on-axis specimens, all 3D woven architectures have lower resistance values compared to the off-axis ones which is typically due to the yarns

orientations being along the longitudinal fibre direction rather than the 45º direction. Moreover, the resistance of off-axis specimens seems to be a function of the unit cell size or the density of the binding yarns. ORT specimen has the smallest unit cell of 5 x 5 mm^2, while both LTL and AI have larger unit cells of 10 x 7 mm^2 and 20 x 25 mm^2, respectively.

In addition to Table 4 for the 3D woven specimens, the through thickness resistance of specimens was evaluated using a 2-probe technique and in all cases it was less than 1 ohm (1Ω). So, the ratio between the through-thickness conductivity and the longitudinal conductivity is approximately "10^{-1}" as opposed to "10^{-4}" for laminated composites [34]. In other words, through-thickness conductivity in 2D laminates is much lower than 3D woven composites. This observation highlights the effect of the z-binding yarns in creating a conduction path/network for the current to flow in the through-thickness direction. Thus, it is expected to have good current penetration within the sample as studied in [36,48], and this ensures that the measured resistance using 4-probe technique is actually representative volume resistivity.

4.2 Electrical resistance in warp (on-axis) direction under monotonic loading

The global stress strain response for all the 3D woven composite architectures, tested along the warp direction, features almost a linear elastic behaviour up to fracture (see Fig. 5a-c). Previous studies [19,20,22] have proven, experimentally, that the damage and cracking progression in 3D woven composites is quite similar to those of cross-ply laminates when loaded along the warp or the weft directions. The damage starts first at the interlacement points between the z-binder and the in-plane yarns "warp and weft". Following this stress localisation effect, in-plane yarns, perpendicular to the loading direction, start experiencing transverse cracking. This is characterised by cracks spanning the whole yarn length and multiplying in number within the yarn up to a saturation point. The damage mechanism changes to delamination between the in-plane yarns that happens at a very last stage of the loading right before the longitudinal fibre breakage of the yarns.

From the electrical resistance point of view, those damage mechanisms, detailed above, result in resistance increase due to the loss of the conduction path within the composite. For on-axis loading of composite materials, damage does not start from the beginning. However, damage initiation occurs within a range of strain values, as detailed in

literature earlier in [20,49] using acoustic emission (AE) sensors, which is referred to here as Crack Onset Strain (COS). This COS value is an architecture dependent as depicted in Fig. 5a-c.

The normalised resistance variation ($\Delta R/R_o$) is defined as the difference between the resistance of the damaged state (R) and the original state (R_o) divided by the original resistance (R_o). In the case of the on-axis specimens (Fig. 5a-c), it is in the range of (15 - 20 %); and it is within the same range for all the tested specimens. This relative resistance increase is due to the fact that the main conductivity path in the on-axis specimens is the longitudinal and binder yarns while damage may occur in the transverse yarns in the form of transverse cracking and matrix diffused damage. These types of damage do not significantly affect the main conduction path for the current and consequently the overall resistance variation as depicted in Fig. 5a-c. However, still this resistance increase can be detected by the electrical resistance monitoring technique. In other words, it is high enough to be captured by the proposed technique.

4.3 Electrical resistance in bias (off-axis) direction under monotonic loading

Stress-strain curves of 3D woven composites loaded in off-axis direction (45º) are characterised by a bilinear response (see Fig. 6a-c & Fig. 7a). The "knee point" is defined as the transition point from the first linear to the second linear regime. The first linear response is governed by the elastic state of the material in which no damage is experienced. Similar to angle ply laminate case reported in [50] this second linear curve is associated with matrix cracking and inter-yarn matrix delamination that leads to gradual change of stiffness. Out of the three architectures investigated in this study, only the ORT architecture exhibits larger deformation and higher strain-to-failure. This tendency of accommodating larger deformation can be correlated to the yarns reorientation (fibre rotation) towards the loading direction. This realignment nature of the ORT architecture was captured by the electrical resistance monitoring technique as shown in Fig. 6a. At a specific strain value, around 17 % strain, the resistance drops drastically indicating a more efficient conduction path in the ORT architecture. This can be attributed to the higher reorientation angle of yarns during testing which has been previously reported in [25]. As a general observation and unlike the on-axis tested specimens, there is no clear COS value for resistance increase.

This suggests that the damage of 3D woven composites in off-axis loading starts from the very beginning of the test.

Fig. 6d shows the representative curve of resistance of three specimens. The resistance variation, in the shaded area, (Fig. 6d) suggests that loss of conductivity is higher in LTL followed by AI and finally ORT. This can be correlated with the level of damage in the different architectures. At the same loading level in this reported region, LTL have more damage followed by AI and finally ORT. To validate this point, an interrupted test (at several load levels) was performed on the three architectures, and the underlying damage mechanisms were observed by X-ray tomography (X-Tex XTH 225 cone-beam tomograph). Two stress levels (Points B and C) from the off-axis stress-strain curve of 3D woven composites were selected (see Fig. 7a). The region of interest (ROI) is the centre of the specimen. Point A denotes zero stress where non-damage specimen was scanned by X-ray as a reference. Point B was selected at the linear elastic segment (approximately 60 MPa) in order to characterise the damage initiation before the "knee point". Point C was around 110 MPa, which is a point after the knee point where damage progression was investigated. X-ray images were captured with X-ray setting of 35 kV and 310 μA. To formalise the damage analysis using X-ray, nomenclature of damage types is given in Table 5.

Note: In Table 5, the F-type starts at the free edge of the specimen while the T-type occurs within yarns and it might start from the free-edge or inside the specimen.

At Point A, no damage due to manufacturing is observed by X-ray. After the specimen was loaded to 60 MPa, the first damage characteristic at Point B observed in all architectures is free-edge matrix cracking (F-type). Damage at Point B is caused by the inter-laminar stresses between layers as reported in [51–53]. Increasing the applied stress, F-type cracks propagate towards the centre of the specimens. Reaching Point C, three damage types are identified (see Fig. 7b). ORT and AI specimens exhibited binder-induced damage (Z-type) at the interlacement points between the in-plane yarns and the binding yarns. Transverse cracking (T-type) within yarns starts to multiply in number especially in the AI specimens. This explains the higher increase of resistance of the AI architecture compared to the ORT counterpart. The (D-type) damage is driven by the in-plane yarns

realignment and rotation towards the loading axis. In the case of the LTL specimens, accumulation of the (D-type) cracks is more severe as it has the least strength (~130 MPa) while no Z-type damage can be observed. This leads to an extensive localised damage which directly results in higher resistance for LTL as captured by the ERM technique.

4.4 Electrical resistance in bias (off-axis) direction under cyclic loading

ORT specimens demonstrate a constant resistance during the unloading cycles with a slight recovery of conductivity. However, there is a tendency to recover conductivity in the beginning of the consecutive loading cycles. In Fig. 8a, the resistance curve drops to a minimum and starts increasing again in every loading cycle. This trend is repeatable for all the tested specimens and the different architectures as it will be detailed later. A closer investigation is detailed in Fig. 9 by zooming into the last unloading/reloading cycle in Fig. 8a.

The cyclic curves (see Fig. 8b) show no resistance variation during the unloading cycles. In addition, the resistance increase during the reloading cycles does not exceed the maximum value of the previous cycle until the maximum stress of the preceding cycle is reached. In the last unloading cycle, although the stress level reaches almost zero stress, the resistance variation (Fig. 8b) remains approximately 40%. The ultimate resistance increase after removing the applied load proves that this resistance increase is due to induced damage in the tested specimen, not due to piezo-resistive effect. In other words, the change of resistance is irreversible due to actual damage in the material.

In the case of cyclic loading, it is quite convenient to differentiate between the behaviour of the lower cycles (1^{st} and 2^{nd}) corresponding to loading within the elastic regime and the higher cycles (3^{rd} to 5^{th}) corresponding to the non-linear regime in which damage effect is significant. In the lower cycles, the increase/decrease in ER during loading/unloading could just be the effect of strain and yarns reorientation in elastic regime. Thus, the first two cycles can be deemed reversible based on the fact that the hysteresis loops of the first and second cycles are identical (see Fig. 8b). For the higher cycles, the last cycle highlighted in Fig. 9 is divided into three main stages I, II and III. The first stage (I), while unloading, represents the irreversible ER change due to the induced damage. This is characterised by almost a constant resistance with a minor reduction while unloading. Upon

reloading in stages (II) and (III), there is a competition between two mechanisms; one of them results in recovery of conductivity "yarns realignment", while the other leads to degradation of conductivity "induced damage". In the second stage (II), it is obvious that the effect of yarns reorientation towards the loading direction is higher than the effect of the induced damage, so there is a recovery of the conduction path/ network which is directly indicated by the resistance reduction to a minimum value. So in spite of damage existence, some resistance reversibility occurs. This competition, between the reorientation "realignment" of yarns and damage accumulation, is reversed, half way through the loading cycle, where the resistance starts increasing again from the minimum value to a higher value compared to the previous loading cycle. This simply demonstrates that the effect of the excessive induced damage during the current cycle is more dominant than the effect of the yarns' realignment that tries to recover the conduction network.

Similarly, the AI specimens tested demonstrated the same trend as the ORT specimens. It is clear from Fig. 10a that AI specimens demonstrate a constant resistance during the unloading cycles with a slight decrease; while there is a tendency of the resistance to decrease even further in the beginning of the consecutive loading cycles. This behaviour can be explained in the same manner as for the ORT specimens. In addition, for the cyclic curves, both remarks regarding the constant resistance upon unloading and the resistance increase every reloading cycle are still valid (see Fig. 10b). The only difference here is in the final change of resistance after unloading which is around 60% in this case compared to 40% in the case of ORT.

For LTL specimens, the same trend of minor resistance change (less than 5%) while unloading and conductivity recovery upon reloading is shown in Fig. 11a. However, there is one major difference compared to the ORT and AI specimens. The resistance variation ($\Delta R/R_o$) is much higher (~ 200%) compared to the other architectures (~ 40% and 60% for ORT and AI respectively). This is attributed to the fact that damage occurs in a localised region for the LTL specimens (Fig. 12) starting from the third cycle. The level of damage induced in the LTL specimens after this cycle leads to extensive localised damage level in the region of interest of LTL specimen results in high resistance measurement. In other words, the localised necking is the cause of the earlier failure of LTL architecture [25].

In order to understand the evolution of damage and plasticity in 3D woven composites tested in off-axis direction, results from the cyclic "load/unload" test are investigated. A schematic is shown in Fig. 13a to explain the calculation of the following parameters.

- E_0: the initial tensile modulus of the tested specimen
- E_i: the tensile modulus at a given cycle (i)
- d_i: the damage level at a given cycle (i)
- ε_i^e: the elastic strain after unloading at a given cycle (i)
- ε_i^p: the residual plastic strain after unloading at a given cycle (i)

The initial modulus (E_0) for all the architectures is determined by measuring the slope of the stress strain curve in the first loading stage; while the reduced tensile modulus "secant modulus" for a given cycle (i) is determined from the unloading curve [54] as shown in Fig. 13a. The evolution of the tensile modulus as well as the residual plastic strain and the normalised resistance variation as function of the "loading/unloading" cycle is reported in Table 6.

As the LTL architecture has the least undulation followed by AI and finally ORT, it demonstrates the highest initial modulus followed by AI and ORT. However, once damage accumulates, the LTL architecture experiences more delamination and slippage between in-plane yarns which is directly reflected in the reduction of the modulus especially at the last cycle. Due to through-thickness binder existence, AI and ORT experience less damage compared to LTL. Moreover, as the ORT unit cell is smaller than that of AI and the ORT binder density is much higher, ORT binding yarns can resist delamination so it maintains the highest modulus, the least damage level and the lowest plastic strain after unloading at the last cycle. Similarly, the change of resistance as a function of the damage level (Fig. 13b) supports the fact that LTL experiences more damage followed by AI and ORT which is directly indicated by the resistance increase.

5 Concluding remarks

Through a systematic experimental study, the effect of the through-thickness binder has been revealed. It has been demonstrated that the initial resistance of the 3D woven specimens are architecture dependent and different from that of 2D laminated composites. For on-axis loaded specimens although the conductivity is mainly due to the contribution of the longitudinal fibres, the resistance increase due to damage in the transverse yarns and delamination can still be detected using the 4-probe technique as the resistance increase is around 20%. On the contrary, the resistance increase for the off-axis loaded specimens is much higher than on-axis counterparts as it reaches approximately 90%. Out of all the 3D woven architectures, ORT loaded off-axially exhibits a recovery in electrical conductivity which indicates that yarns realignment reached a point where they become connected again and resistance drops accordingly. For all the off-axis tested specimens, the resistance increase upon unloading is irreversible which proves that the resistance increase is due to actual damage in the tested specimens, not due to piezo-resistive effect. In cyclic loading tests, during unloading the resistance drop is small due to the piezo-resistivity nature. However, during reloading the resistance drops due to fibre/yarns realignment up to a point at which the effect of induced damage becomes more significant than the recovery due to the realignment process. That is why the resistance starts increasing again. The remaining challenge for ERM would be the ability to accurately locate and identify the size of the damage in 3D woven composites and correlate the measured resistance variation to the internal level of damage. At the moment, it is very difficult to obtain a direct correlation between resistance variation and damage in 3D woven composites due to the complexity of the conduction path along the three orthogonal directions (x, y & z). Further work needs to be considered to support the resistance change with AE damage accumulation detection or *in-situ* X-ray CT scans. Thus, this study represents an explanatory paper to demonstrate the potential of using ERM for damage detection in 3D woven carbon fibre-based composites and highlight the challenges that need to be overcome to be able to establish ERM as a SHM technique for such material systems.

6 Acknowledgments

Authors would like to acknowledge the financial support from University of Manchester (UoM) and from Baseline Research Funds from King Abdullah University of Science and Technology (KAUST). We also acknowledge the technical support from the Northwest Composites Certification and Evaluation Facility (NCCEF).

List of Figures:

List of Tables:

References

[1] Mcclain M, Senior R, Organic TE, Composites M. Overview of Recent Developments in 3D Structures. Albany Eng Compos 2012:1–12.

[2] Gerlach R, Siviour CR, Wiegand J, Petrinic N. In-plane and through-thickness properties, failure modes, damage and delamination in 3D woven carbon fibre composites subjected to impact loading. Compos Sci Technol 2012;72:397–411. doi:10.1016/j.compscitech.2011.11.032.

[3] Hao A, Sun B, Qiu Y, Gu B. Dynamic properties of 3-D orthogonal woven composite T-beam under transverse impact. Compos Part A Appl Sci Manuf 2008;39:1073–82. doi:10.1016/j.compositesa.2008.04.012.

[4] Ji C, Sun B, Qiu Y, Gu B. Impact damage of 3D orthogonal woven composite circular plates. Appl Compos Mater 2007;14:343–62. doi:10.1007/s10443-008-9050-x.

[5] Luo Y, Lv L, Sun B, Qiu Y, Gu B. Transverse impact behavior and energy absorption of three-dimensional orthogonal hybrid woven composites. Compos Struct 2007;81:202–9. doi:10.1016/j.compstruct.2006.08.011.

[6] Seltzer R, González C, Muñoz R, Llorca J, Blanco-Varela T. X-ray microtomography analysis of the damage micromechanisms in 3D woven composites under low-velocity impact. Compos Part A Appl Sci Manuf 2013;45:49–60. doi:10.1016/j.compositesa.2012.09.017.

[7] Stig F, Hallström S. Influence of crimp on 3D-woven fibre reinforced composites. Compos Struct 2013;95:114–22. doi:10.1016/j.compstruct.2012.07.022.

[8] Stig F, Hallström S. Assessment of the mechanical properties of a new 3D woven fibre composite material. Compos Sci Technol 2009;69:1686–92. doi:10.1016/j.compscitech.2008.04.047.

[9] L. Tong, A.P. Mouritz MB. Chapter 5 3D Woven Composites. 3D Fibre Reinf. Polym. Compos., 2009.

[10] Varna J, Berglund LA, Ericson ML. Transverse single-fibre test for interfacial debonding in composites: 2. Modelling. Compos Part A Appl Sci Manuf 1997;28:317–26. doi:10.1016/S1359-835X(96)00125-X.

[11] Lubineau G, Ladeve P. On a damage mesomodel for laminates : micro – meso relationships , possibilities and limits. Compos Sci Technol 2001;61:2149–58.

[12] Lubineau G. A Pyramidal Modeling Scheme for Laminates - Identification of Transverse Cracking. Int J Damage Mech 2010;19:499–518. doi:10.1177/1056789509102725.

[13] Nouri H, Lubineau G, Traudes D. An experimental investigation of the effect of shear-induced diffuse damage on transverse cracking in carbon-fiber reinforced

laminates. Compos Struct 2013;106:529–36. doi:10.1016/j.compstruct.2013.06.026.

[14] Zhang J, Fan J, Herrmann KP. Delaminations induced by constrained transverse cracking in symmetric composite laminates. Int J Solids Struct 1999;36:813–46. doi:10.1016/S0020-7683(97)00325-9.

[15] Nairn J, Hu S. The initiation and growth of delamination induced by matrix microcracks in laminated composites. Int J Fract 1991;24:1–24.

[16] Ladèveze P, Lubineau G. An enhanced mesomodel for laminates based on micromechanics. Compos Sci Technol 2002;62:533–41. doi:10.1016/S0266-3538(01)00145-2.

[17] Beetz CP. The analysis of carbon fibre strength distributions exhibiting multiple modes of failure. Fibre Sci Technol 1982;16:45–59. doi:10.1016/0015-0568(82)90015-X.

[18] Chi Z, Chou TW, Shen G. Determination of single fibre strength distribution from fibre bundle testings. J Mater Sci 1984;19:3319–24. doi:10.1007/BF00549820.

[19] Yu B, Bradley RS, Soutis C, Hogg PJ, Withers PJ. 2D and 3D imaging of fatigue failure mechanisms of 3D woven composites. Compos Part A Appl Sci Manuf 2015;77:37–49. doi:10.1016/j.compositesa.2015.06.013.

[20] Lomov S V, Bogdanovich AE, Karahan M, Mungalov D, Verpoest I. Mechanical Behaviour of Non-crimp 3D Woven Carbon/Epoxy Composite Under in-plane Tensile Loading. 18th Int Conf Compos Mater 2011:1–5.

[21] Ansar M, Xinwei W, Chouwei Z. Modeling strategies of 3D woven composites: A review. Compos Struct 2011;93:1947–63. doi:10.1016/j.compstruct.2011.03.010.

[22] Dai S, Cunningham PR, Marshall S, Silva C. Influence of fibre architecture on the tensile, compressive and flexural behaviour of 3D woven composites. Compos Part A Appl Sci Manuf 2015;69:195–207. doi:10.1016/j.compositesa.2014.11.012.

[23] Saleh MN, Wang Y, Yudhanto A, Joesbury A, Potluri P, Lubineau G, et al. Investigating the Potential of Using Off-Axis 3D Woven Composites in Composite Joints' Applications. Appl Compos Mater 2016;24:377–96. doi:10.1007/s10443-016-9529-9.

[24] Gresil M, Saleh MN, Soutis C. Transverse Crack Detection in 3D Angle Interlock Glass Fibre Composites Using Acoustic Emission. Materials (Basel) 2016;9. doi:10.3390/ma9080699.

[25] Saleh MN, Yudhanto A, Potluri P, Lubineau G, Soutis C. Characterising the loading direction sensitivity of 3D woven composites: Effect of z-binder architecture. Compos Part A Appl Sci Manuf 2016;90:577–88. doi:10.1016/j.compositesa.2016.08.028.

[26] Saleh MN, Soutis C. Recent advancements in mechanical characterisation of 3D

woven composites. Mech Adv Mater Mod Process 2017;3. doi:10.1186/s40759-017-0027-z.

[27] Aymerich F, Meili S. Ultrasonic evaluation of matrix damage in impacted composite laminates. Compos Part B Eng 2000;31:1–6. doi:10.1016/S1359-8368(99)00067-0.

[28] Sánchez DM, Gresil M, Soutis C. Distributed internal strain measurement during composite manufacturing using optical fibre sensors. Compos Sci Technol 2015;120:49–57. doi:10.1016/j.compscitech.2015.09.023.

[29] De Rosa IM, Santulli C, Sarasini F. Acoustic emission for monitoring the mechanical behaviour of natural fibre composites: A literature review. Compos Part A Appl Sci Manuf 2009;40:1456–69. doi:10.1016/j.compositesa.2009.04.030.

[30] Ciang CCC, Lee J-RJ, Bang HH-J. Structural health monitoring for a wind turbine system: a review of damage detection methods. Meas Sci Technol 2008;19:122001. doi:10.1088/0957-0233/19/12/122001.

[31] Ng CT, Veidt M. A Lamb-wave-based technique for damage detection in composite laminates. Smart Mater Struct 2009;18:74006. doi:10.1088/0964-1726/18/7/074006.

[32] Schulte K, Baron C. Load and failure analyses of CFRP laminates by means of electrical resistivity measurements. Compos Sci Technol 1989;36:63–76. doi:10.1016/0266-3538(89)90016-X.

[33] Abry J, Bochard S, Chateauminois A, Salvia M, Giraud G. In situ detection of damage in CFRP laminates by electrical resistance measurements. Compos Sci Technol 1999;59:925–35. doi:10.1016/S0266-3538(98)00132-8.

[34] TODOROKI A, YOSHIDA J. Electrical Resistance Change of Unidirectional CFRP Due to Applied Load. JSME Int J Ser A 2004;47:357–64. doi:10.1299/jsmea.47.357.

[35] Selvakumaran L, Lubineau G. Electrical behavior of laminated composites with intralaminar degradation: A comprehensive micro-meso homogenization procedure. Compos Struct 2014;109:178–88. doi:10.1016/j.compstruct.2013.10.057.

[36] Selvakumaran L, Long Q, Prudhomme S, Lubineau G. On the detectability of transverse cracks in laminated composites using electrical potential change measurements. Compos Struct 2015;121:237–46. doi:10.1016/j.compstruct.2014.11.008.

[37] Song DY, Takeda N, Kitano A. Correlation between mechanical damage behavior and electrical resistance change in CFRP composites as a health monitoring sensor. Mater Sci Eng A 2007;456:286–91. doi:10.1016/j.msea.2006.11.130.

[38] Abry, Choi, Chateauminois, Dalloz, Giraud, Salvia. In-situ monitoring of damage in CFRP laminates by menas of AC and DC measurement. Compos Sci Technol 2001;61:855–64.

[39] Ogi K, Takao Y. Characterization of piezoresistance behavior in a CFRP

unidirectional laminate. Compos Sci Technol 2005;65:231–9. doi:10.1016/j.compscitech.2004.07.005.

[40] Omagari K, Todoroki A, Shimamura Y, Kobayashi H. Detection of Matrix Cracking of CFRP Using Electrical Resistance Changes. Key Eng Mater 2005;297–300:2096–101. doi:10.4028/www.scientific.net/KEM.297-300.2096.

[41] Todoroki A, Tanaka Y. Delamination identification of cross-ply graphite / epoxy composite beams using electric resistance change method. Compos Sci Technol 2002;62:629–39. doi:10.1016/S0266-3538(02)00013-1.

[42] Nishio Y, Todoroki A, Mizutani Y, Suzuki Y. Electrical Resistance Change of Interlaminar Woven-Fabric Cfrp in Mode Ii Fracture. 16th Eur. Conf. Compos. Mater., Seville: 2014, p. 22–6.

[43] Nasr Saleh M, Lubineau G. Understanding the mechanisms that change the conductivity of damaged ITO-coated polymeric films: A micro-mechanical investigation. Sol Energy Mater Sol Cells 2014;130:199–207. doi:10.1016/j.solmat.2014.07.011.

[44] Long AC, Brown LP. 8 – Modelling the geometry of textile reinforcements for composites: TexGen. Compos. Reinf. Optim. Perform., 2011, p. 239–64. doi:10.1533/9780857093714.2.239.

[45] Almuhammadi K, Selvakumaran L, Alfano M, Yang Y, Bera TK, Lubineau G. Laser-based surface preparation of composite laminates leads to improved electrodes for electrical measurements. Appl Surf Sci 2015;359:388–97. doi:10.1016/j.apsusc.2015.10.086.

[46] Saleh MN, Lubineau G, Potluri P, Withers PJ, Soutis C. Micro-mechanics based damage mechanics for 3D orthogonal woven composites: Experiment and numerical modelling. Compos Struct 2016;156:115–24. doi:10.1016/j.compstruct.2016.01.021.

[47] Yudhanto A, Lubineau G, Ventura IA, Watanabe N, Iwahori Y, Hoshi H. Damage characteristics in 3D stitched composites with various stitch parameters under in-plane tension. Compos Part A Appl Sci Manuf 2015;71:17–31. doi:10.1016/j.compositesa.2014.12.012.

[48] Selvakumaran L, Lubineau G. Effect of voltage measurement on the quantitative identification of transverse cracks by electrical measurements. Sensors (Switzerland) 2016;16. doi:10.3390/s16040427.

[49] Li L, Lomov S V., Yan X. Correlation of acoustic emission with optically observed damage in a glass/epoxy woven laminate under tensile loading. Compos Struct 2015;123:45–53. doi:10.1016/j.compstruct.2014.12.029.

[50] Fuller JD, Wisnom MR. Pseudo-ductility and damage Suppression in thin ply angle-ply carbon-epoxy laminates. Compos Part A Appl Sci Manuf 2013;69:64–71. doi:10.1016/j.compositesa.2014.11.004.

[51] Mittelstedt C, Becker W. Free-Edge Effects in Composite Laminates. Appl Mech Rev 2007;60:217. doi:10.1115/1.2777169.

[52] Mittelstedt C, Becker W. Interlaminar Stress Concentrations in Layered Structures: Part I - A Selective Literature Survey on the Free-Edge Effect since 1967. J Compos Mater 2004;38:1037–62. doi:10.1177/0021998304040566.

[53] Sun CT, Zhou SG. Failure of Quasi-Isotropic Composite Laminates with Free Edges. J Reinf Plast Compos 1988;7:515–57. doi:10.1177/073168448800700602.

[54] Aguilar Ventura I, Lubineau G. The effect of bulk-resin CNT-enrichment on damage and plasticity in shear-loaded laminated composites. Compos Sci Technol 2013;84:23–30. doi:10.1016/j.compscitech.2013.05.002.

Table 1 Specification of textile architecture of 3D woven composites

Parameter	ORT	LTL	AI
Warp number of layers	8	5	8
Weft number of layers	9	6	9
Warp fibre count	12k	12k	12k
Weft fibre count	12k	12k	12k
z-binder fibre count	6k	12k	6k
Ends/cm (warp)	31.52	17.73	31.52
Picks/cm (weft)	38	36	34
Binders/cm (z-binder)	3.94	17.73	3.94
Areal density (g/m^2)	3353	3260	3044

Table 2 Volume fraction of constituents (fibre, matrix, void) in 3D woven composites

Constituent	3D composite		
	ORT	LTL	AI
Fibre (%)	51.35 ± 0.45	59.16 ± 0.24	55.4 ± 0.80
Matrix (%)	46.02 ± 0.43	39.21 ± 0.14	42.18 ± 0.97
Voids (%)	2.63 ± 0.02	1.63 ± 0.13	2.42 ± 0.19

Table 3 Directional fibre volume fraction in 3D woven composites

Direction of fibre tow	ORT	LTL	AI
Warp (%)	21.57	14.36	25.58
Weft (%)	26.00	29.15	27.59
z-binder (%)	3.77	15.65	2.22

Table 4 Initial resistance for tested architectures in ohms

Architecture	Off-axis	On-axis
	Bias (45º)	Warp (0º)
ORT	0.094 ± 0.012	0.080 ± 0.001
LTL	0.110 ± 0.001	0.076 ± 0.004
AI	0.129 ± 0.008	0.065 ± 0.001

Table 5 Nomenclature of damage types

Code	Damage type
F	Free edge matrix crack between yarns
Z	Z-binder induced damage
T	Transverse crack within yarns
D	Inter-yarn matrix delamination

Table 6 Modulus and plastic strain evolution as function of the loading cycles

Cycle	Modulus (GPa)			Plastic strain (%)			$\Delta R/R_0$		
	ORT	AI	LTL	ORT	AI	LTL	ORT	AI	LTL
Initial	11.97	12.07	13.08	0	0	0	0	0	0
1st	7.84	7.87	7.95	1.21	1.13	1.42	0.08	0.02	0.1
2nd	6.67	6.81	4.59	3.61	3.49	4.61	0.08	0.05	0.23
3rd	5.91	6.53	4.24	5.75	5.96	8.55	0.12	0.13	0.57
4th	5.71	5.5	4.24	7.84	8.08	13.37	0.22	0.33	1.33
5th	5.66	5.39	3.97	9.98	10.78	20.51	0.38	0.67	1.71

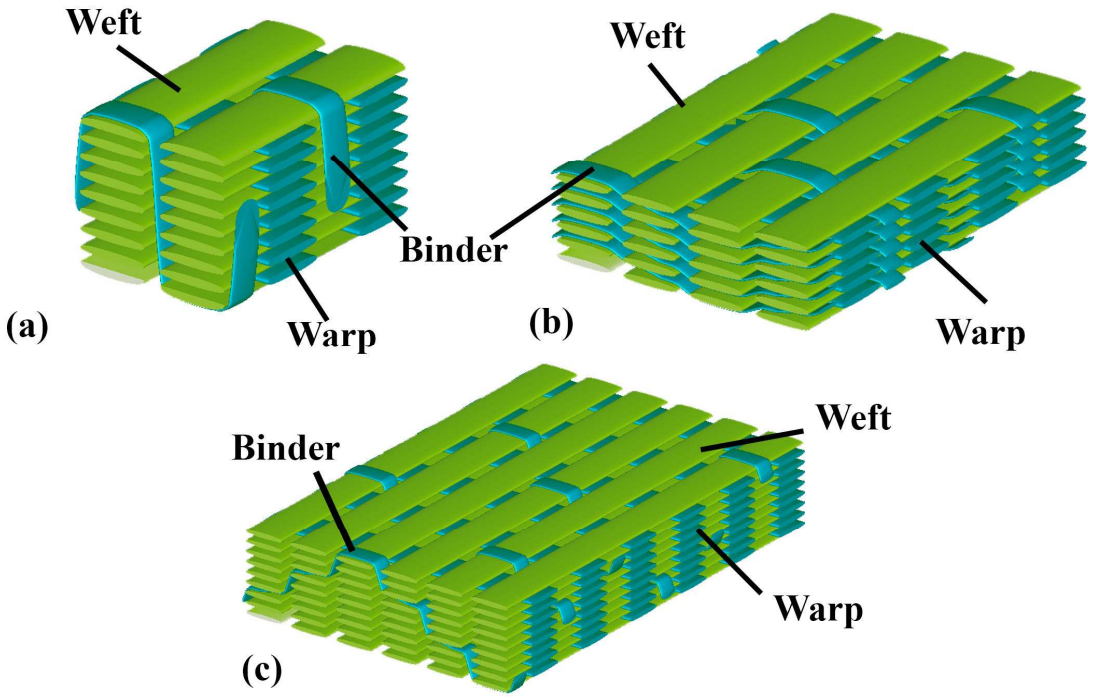

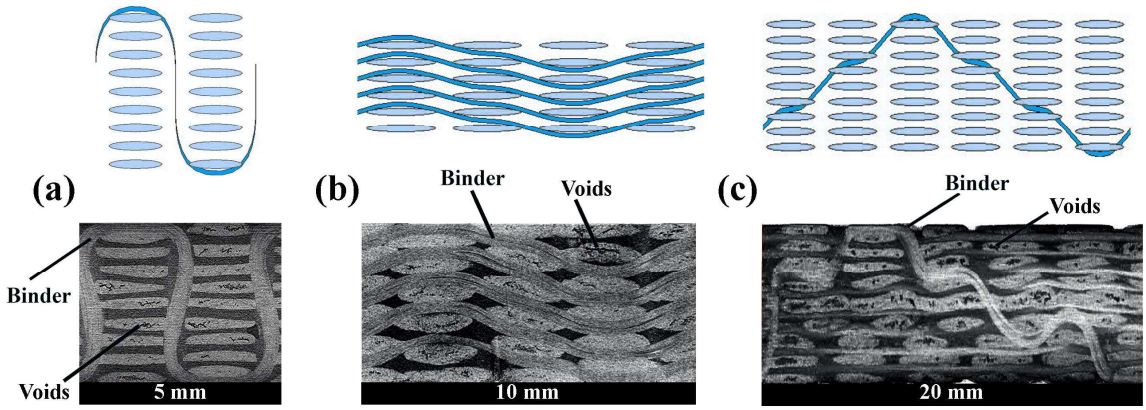

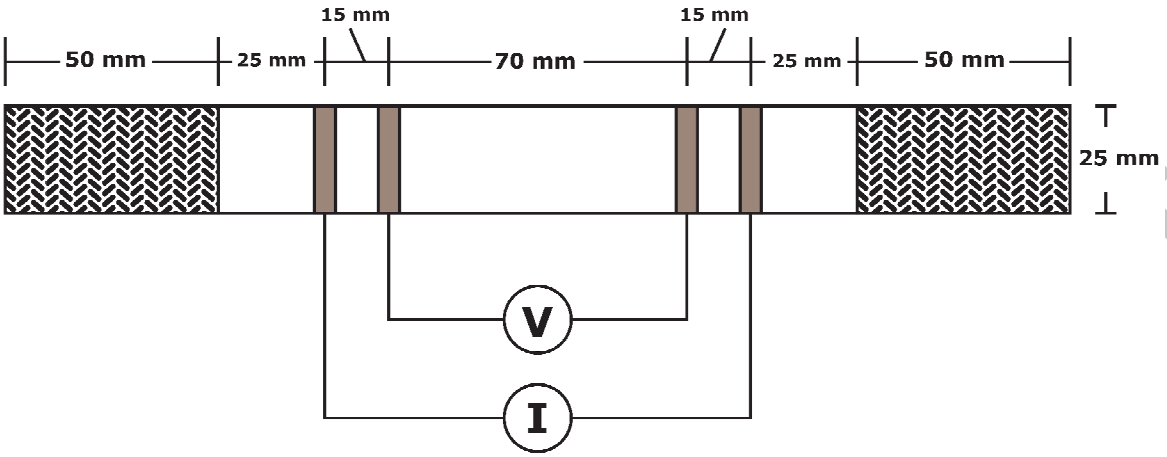

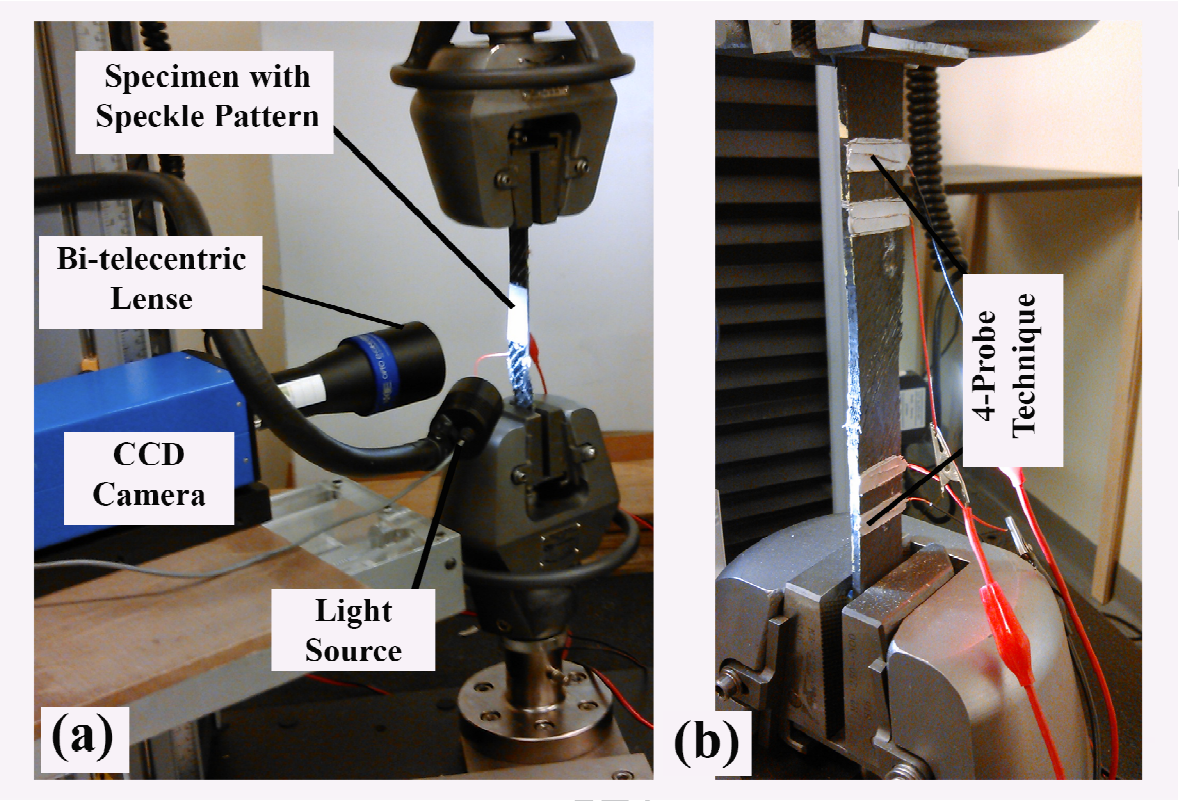

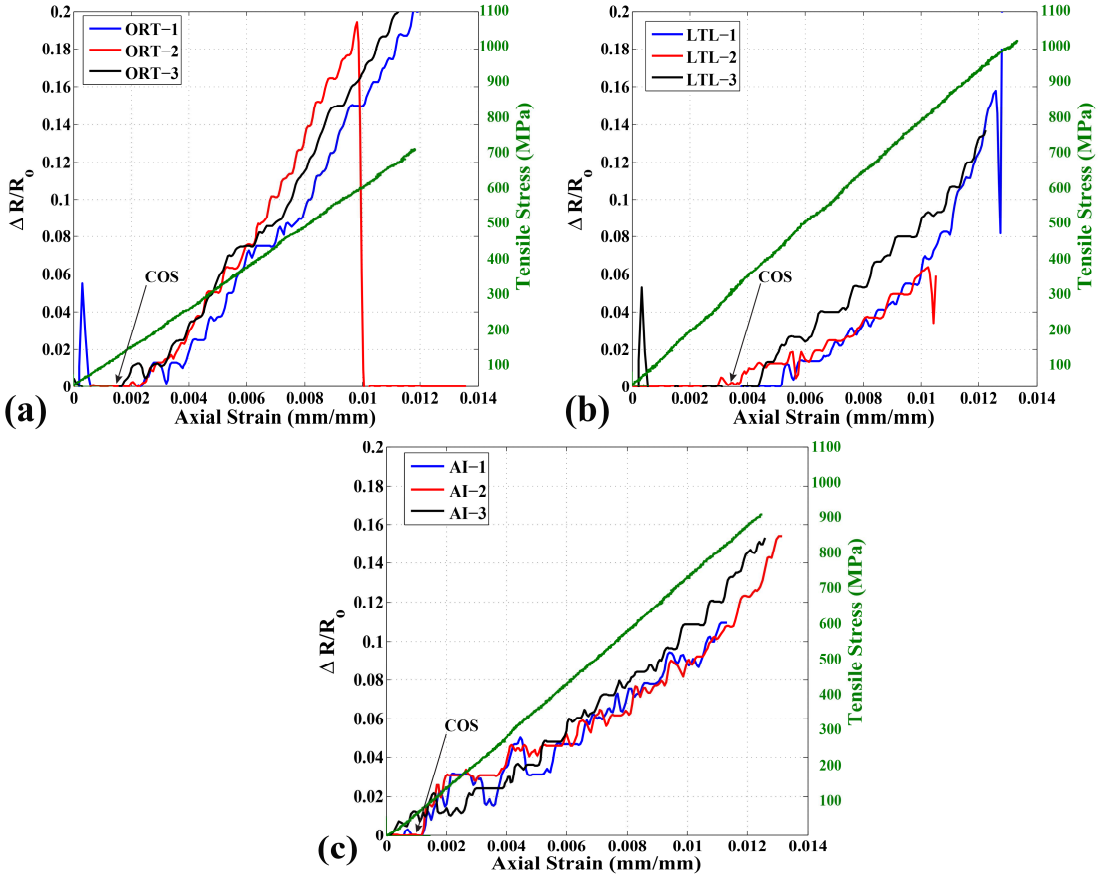

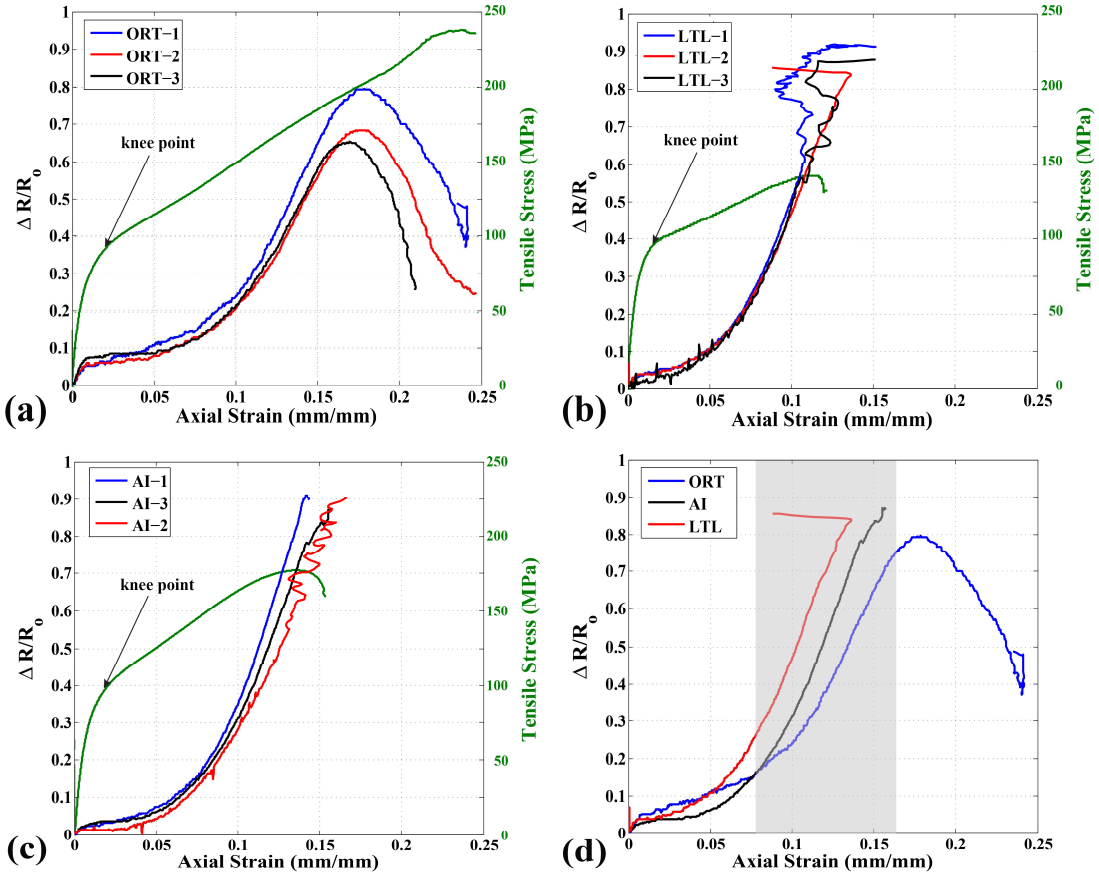

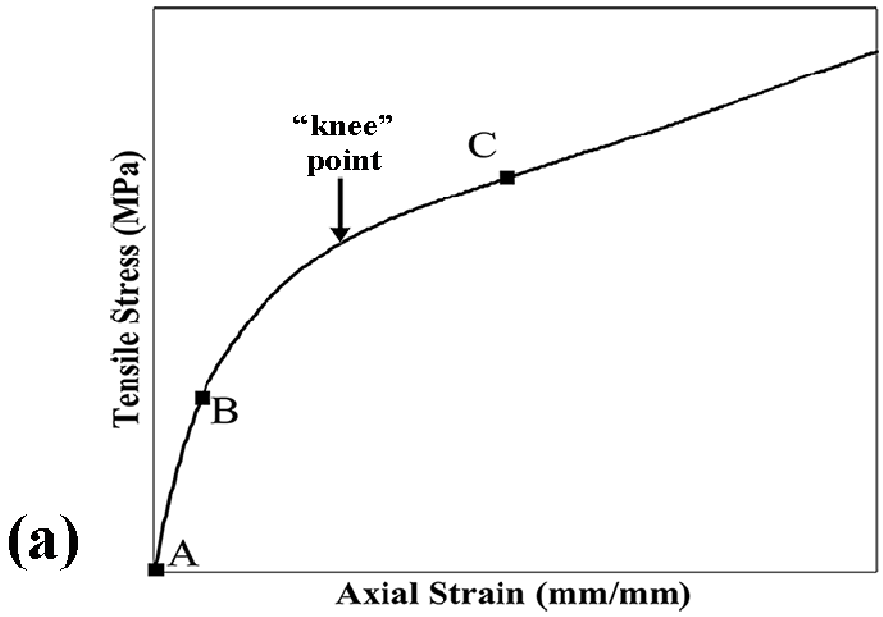
Tensile Stress (MPa)
"knee" point
C
B
A
Axial Strain (mm/mm)

(a)

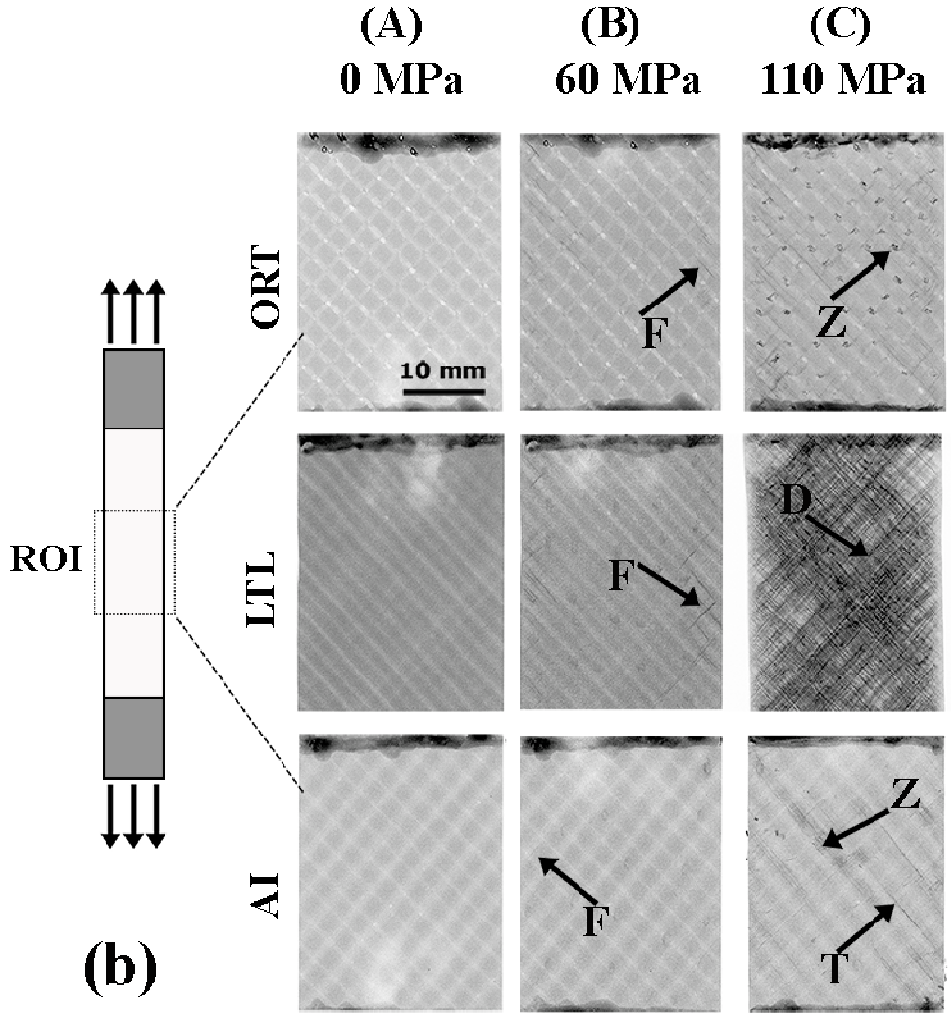
(A)
0 MPa
(B)
60 MPa
(C)
110 MPa
ORT
LTL
AI
ROI
10 mm
F
Z
F
D
F
Z
T

(b)

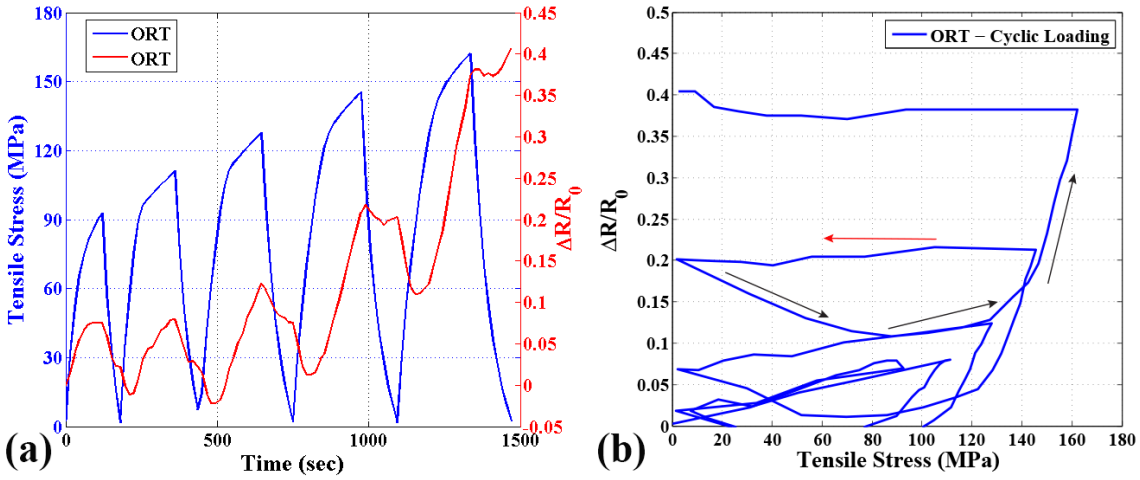

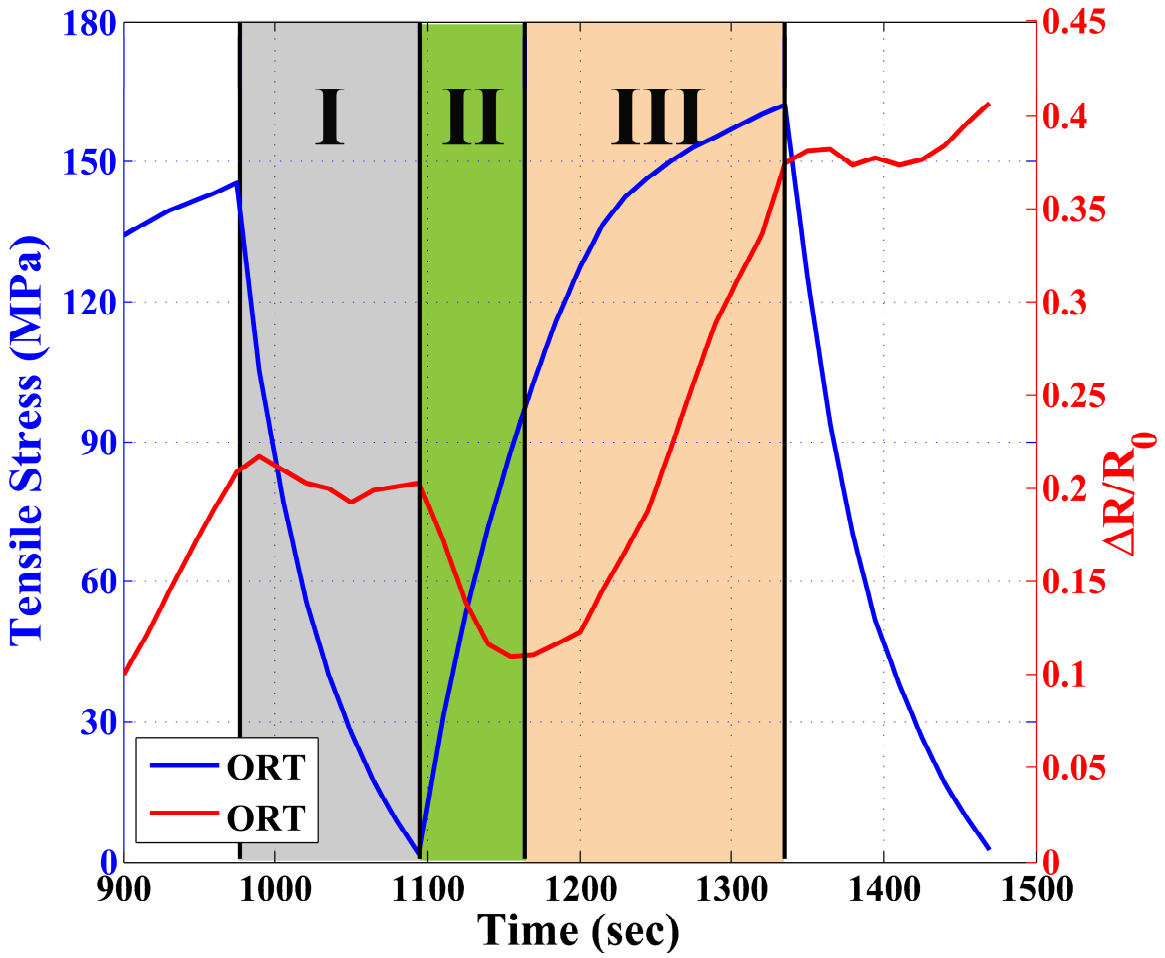
I
II
III
ORT
ORT
Tensile Stress (MPa)
ΔR/R0
Time (sec)
180
150
120
90
60
30
0
0.45
0.4
0.35
0.3
0.25
0.2
0.15
0.1
0.05
0
900
1000
1100
1200
1300
1400
1500